Journal of Controlled Release 364 (2023) 246–260

Contents lists available at ScienceDirect

Journal of Controlled Release

journal homepage: www.elsevier.com/locate/jconrel

Potent inhibition of MMP-9 by a novel sustained-release platform attenuates left ventricular remodeling following myocardial infarction

Amit Itzhar [a,1], Gal Yosef [a,1], Maayan Eilon-Ashkenazy [a,1], Yulia Shmidov [b], Hadas Gil [a], Shiran Lacham-Hartman [a], Sigal Elyagon [c,d], Sharon Etzion [c], Ronit Bitton [b], Smadar Cohen [a,c], Yoram Etzion [c,d,**], Niv Papo [a,e,*]

[a] Avram and Stella Goldstein-Goren Department of Biotechnology Engineering, Ben-Gurion University of the Negev, Beer-Sheva, Israel
[b] Department of Chemical Engineering and the Ilse Katz Institute for Nanoscale Science and Technology, Ben-Gurion University of the Negev, Beer-Sheva, Israel
[c] Regenerative Medicine and Stem Cell (RMSC) Research Center, Ben-Gurion University of the Negev, Beer-Sheva, Israel
[d] Department of Physiology and Cell Biology, Ben-Gurion University of the Negev, Beer-Sheva, Israel
[e] National Institute of Biotechnology, Ben-Gurion University of the Negev, Beer-Sheva, Israel

ARTICLE INFO

Keywords:
Affinity-based delivery system
Alginate sulfate
Protein engineering
Heparin-binding peptide
Matrix metalloproteinase
Myocardial infarction

ABSTRACT

Sustained drug-release systems prolong the retention of therapeutic drugs within target tissues to alleviate the need for repeated drug administration. Two major caveats of the current systems are that the release rate and the timing cannot be predicted or fine-tuned because they rely on uncontrolled environmental conditions and that the system must be redesigned for each drug and treatment regime because the drug is bound *via* interactions that are specific to its structure and composition. We present a controlled and universal sustained drug-release system, which comprises minute spherical particles in which a therapeutic protein is affinity-bound to alginate sulfate (AlgS) through one or more short heparin-binding peptide (HBP) sequence repeats. Employing post-myocardial infarction (MI) heart remodeling as a case study, we show that the release of C9—a matrix metalloproteinase-9 (MMP-9) inhibitor protein that we easily bound to AlgS by adding one, two, or three HBP repeats to its sequence—can be directly controlled by modifying the number of HBP repeats. In an *in vivo* study, we directly injected AlgS particles, which were bound to C9 through three HBP repeats, into the left ventricular myocardium of mice following MI. We found that the particles substantially reduced post-MI remodeling, attesting to the sustained, local release of the drug within the tissue. As the number of HBP repeats controls the rate of drug release from the AlgS particles, and since C9 can be easily replaced with almost any protein, our tunable sustained-release system can readily accommodate a wide range of protein-based treatments.

1. Introduction

Sustained drug-release systems enhance therapeutic efficacy and reduce off-target toxicity by locally prolonging the retention of drugs within their target sites. As such, these systems are suitable for local, long-term treatments, especially when the target molecule demonstrates delayed expression at the site or when repeated administration is required but access to the target organ is restricted [1–3]. Notwithstanding their clear medical benefits, most currently available sustained drug-release systems suffer from two significant caveats. First, the drug-

Abbreviations: AlgS, alginate sulfate; APMA, 4-aminophenylmercuric acetate; BGU, Ben-Gurion University of the Negev; Cryo-TEM, cryo-transmission electron microscopy; d_h, hydrodynamic diameter; DLS, dynamic light scattering; ECM, extracellular matrix; EF, ejection fraction; FA, formaldehyde; HBP, heparin-binding peptide; i.p, intraperitoneal; IPTG, isopropyl b-D-1-thiogalactopyranoside; K_D, equilibrium binding constant; Ki, inhibition constant; LAD, left anterior descending; LV, left ventricle; LVEDV, LV end-diastolic volume; LVESV, LV end-systolic volume; MI, myocardial infarction; MMP, matrix metalloproteinase; $MMP\text{-}9_{CAT}$, MMP-9 catalytic domain; $MMP\text{-}9_{FL}$, full-length MMP-9; PBS, phosphate buffered saline; PMSF, phenylmethylsulfonyl fluoride; RU, response units; SAXS, small-angle X-ray scattering; SDS-PAGE, sodium dodecyl sulfate–polyacrylamide gel electrophoresis; SEM, standard error of the mean; SPR, surface plasmon resonance; SD, standard deviation; TIMP, tissue inhibitor of metalloproteinase..

* Correspondence to: N. Papo, Department of Biotechnology Engineering, Ben-Gurion University of the Negev, Beer-Sheva, Israel.
** Correspondence to Y Etzion, Department of Physiology and Cell Biology, Ben-Gurion University of the Negev, Beer-Sheva, Israel.
E-mail addresses: tzion@bgu.ac.il (Y. Etzion), papo@bgu.ac.il (N. Papo).
[1] Equal contribution

https://doi.org/10.1016/j.jconrel.2023.10.033
Received 17 July 2023; Received in revised form 3 October 2023; Accepted 20 October 2023

release mechanism is usually complex and relies on uncontrolled environmental conditions (*e.g.*, enzymatic activity in the target tissue), such that the drug-release rate is often unpredictable and cannot be tightly controlled or tuned [2–9]. Second, the drug is typically bound to the delivery system through specific drug–target interactions (*e.g.*, hydrogen bonds, hydrophobic or electrostatic interactions) that are dictated by the structure and composition of each drug used [3–5]. Therefore, these systems are not universal and must be designed or redesigned for each required drug and treatment regime. Here, to overcome these two limitations, we developed a sustained drug-release system that both (a) enables accurate predictability and tight drug-release control, and (b) can be easily adjusted to accommodate a wide range of protein-based therapeutic drugs. As a treatment case study, we chose myocardial infarction (MI), wherein the target organ (the heart) is difficult to access and drug-release predictability and control are critical for treatment success.

Extensive MI is followed by marked extracellular matrix (ECM) degradation, which typically manifests as progressive cardiac remodeling, namely, in changes in the shape and function of the heart [10]. Such progressive remodeling hampers cardiac function and often leads to severe heart failure [11,12], which is one of the leading causes of death, worldwide [13,14]. The main driver of the MI-induced ECM degradation is the proteolytic activity of matrix metalloproteinases (MMPs)—a family of 23 endopeptidases [15] whose proteolytic activity is endogenously regulated by the tissue inhibitors of metalloproteinases (TIMPs). Notably, MI considerably increases the expression levels of MMPs in inflammatory cells [16–18], whereas the levels of TIMPs remain unchanged in the cardiac fibroblasts [19,20]. Thus, an imbalance between MMP and TIMP expression levels is associated with post-MI ECM degradation, and the magnitude of this imbalance can affect the severity of post-MI cardiac remodeling [5,21–25]. For example, while the plasma levels of MMP-9 were found to increase by >200% one day following an MI event (reaching a peak three days following the event), the levels of the MMP inhibitor TIMP-2 remained unchanged [21]. The consequent uncontrolled proteolytic activity of MMP-9 [26] exacerbates tissue remodeling and left-ventricular (LV) dysfunction [24,27]; therefore, balancing MMP-9 activity during the critical days following an MI event (*i.e.*, 2–4 days post-MI [21]) may be the key to preventing cardiac remodeling and its detrimental consequences.

Most attempts to externally regulate post-MI MMP activity by repeatedly administering therapeutic drugs have been unsuccessful [28–30]. A potential alternative to repeated administration [4–6] is to bind the drug to a suitable biomaterial and deliver it directly to the heart [31,32], preferably by using injectable biomaterials, such as hydrogels or nanoparticles [31,33,34]. However, the drug-release timing in available systems cannot be reliably predicted or tightly controlled [2–9], which may lead to unwanted side effects, particularly when the released drug may bind multiple targets [3–6].

To overcome these limitations, we propose to fabricate an affinity-based release system that utilizes alginate sulfate (AlgS)—a non-immunogenic synthetic biomaterial that serves as the building block for various controlled-release systems [2,35,36]. AlgS is created by sulfating the uronic acid monomers of the natural, plant-derived polysaccharide alginate, in a process that depolymerizes the alginate molecule (from 100 kDa to 10 kDa) without affecting its chemical properties [36]. In the current study, we chose to use AlgS as our delivery system because it is highly stable, biocompatible (namely, AlgS chains have been shown to be cytocompatible in various cell lines [37]), bio-eliminable (namely, it is excreted through the kidneys [37]), and shows gentle gelling properties that enable the encapsulation and retention of fragile molecules, such as peptides and proteins, in their active forms [35]. Importantly, the sulfonation process yields multiple affinity binding sites in AlgS, and the resulting chains mimic heparin/heparan sulfate chains; these chains, in turn, bind heparin-binding peptides (HBPs), namely, peptides with the sequence G_4SPPRRARVTY, which is found in various growth factors, cytokines, chemokines, and cell-adhesion molecules [36,38–40]. Notably, the HBP can be easily fused to any protein to yield nano- and micro-particles that contain complexes of protein–HBP and AlgS (designated protein–HBP–AlgS). Such particles should be highly advantageous as injectable sustained drug-release systems because AlgS is not immunogenic or recognized by enzymes in the human body [38], and, therefore, the AlgS-bound protein is released only according to the binding equilibrium between the HBP and AlgS [2,35,36,38,41]. By modulating the HBP–AlgS equilibrium binding constant—*e.g.*, by changing the number of HBP repeating units—and injecting the protein–HBP–AlgS particles into the target tissue, the HBP-bound protein could be locally released in a slow, predictable, and tightly controlled manner, which can dramatically increase treatment efficacy and clinical outcomes [35,42]. However, while proteins that naturally contain HBP domains have been explored as potential therapeutics with sustained release from AlgS platform [35], the recombinant addition of HBP domains to proteins that do not naturally contain this sequence has not been examined as a means of generating a "universal", finely controlled sustained drug-release system.

To test this concept in the context of MI, we utilized a high-affinity, high-selectivity potent inhibitor of the MMP-9 catalytic domain (MMP-9_{CAT}), termed C9, which we previously developed by modifying the non-specific MMP inhibitor, N-TIMP2 [43]. Since small proteins such as C9 (17.1 kDa) are expected to demonstrate a short tissue-retention time [2], they are unsuitable as therapeutic drugs; however, they are highly suitable as the active components in sustained-release systems. Therefore, we fused C9 to one, two, or three HBP repeats, resulting in C9–HBP1/2/3–AlgS particles, respectively. We hypothesized that injecting these particles directly into the myocardium would induce the local and sustained release of the C9–HBP components, thereby optimizing the inhibition of MMP-9 and increasing treatment efficacy following MI [21]. To test this hypothesis, we first conducted an *in vitro* study in which we examined various C9–HBP fusions, each with a different affinity to AlgS, and selected the particles whose size and binding in equilibrium best facilitate the sustained release of the C9–HBP component. Then, we used these particles in *in vivo* trials to select the particles that are retained for the longest period in both skeletal muscle and cardiac tissue. Finally, we injected these selected particles—namely, C9–HBP3–AlgS—*in vivo* into the myocardium of mice after MI and characterized long-term (30 days) recovery, both functionally and morphologically.

2. Materials and methods

2.1. Expression and purification of N-TIMP2 variants and MMP-9_{CAT}

Our previously developed MMP-9 inhibitor, C9, includes seven mutations in the N-$TIMP2_{WT}$ (N-TIMP2 wild-type) gene (see [43]). For the current study, we expressed N-$TIMP2_{WT}$, C9, and C9–HBP1/2/3 (*i.e.*, a C9 molecule fused to either one, two, or three HBP repeats, respectively) in the methylotrophic X33 *Pichia pastoris* yeast strain using an established protocol with some modifications (see [44]). To fuse C9 to HBP and generate the various C9–HBP proteins, we first PCR-amplified the C9 gene by using the forward primer (5'-GGTATCTCTCGAGAAAAGATGCAGCTGCATGCCG-3′) and the reverse primers for C9 and for the C9–HBP1/2/3 clones (5'-TACCAGATGGGCTGCGAGGCGGCCGCCAGC-3′, 5'-TACCAGATGGGCTGCGAGGGTGGAGGCGGCTCCCCACCTAGACGTGCTCGTGTGACTTACGCGGCCGCCAGC-3′, 5'-TACCAGATGGGCTGCGAGGGTGGAGGCGGCTCCCCACCTAGACGTGCTCGTGTGACTTACGGTGGAGGCGGCTCCCCACCTAGACGTGCTCGTGTGACTTACGCGGCCGCCAGC-3′, 5'-TACCAGATGGGCTGCGAGGGTGGAGGCGGCTCCCCACCTAGACGTGCTCGTGTGACTTACGGTGGAGGCGGCTCCCCACCTAGACGTGCTCGTGTGACTTACGGTGGAGGCGGCTCCCCACCTAGACGTGCTCGTGTGACTTACGCGGCCGCCAGC-3′, respectively). For N-$TIMP_{WT}$, we used the primers described in [44]. The *Xho*I and *Not*I restriction enzymes (New England Biolabs, Ipswich, MA) were used to digest the amplified

C9–HBP clones and the pPICZαA vector (Invitrogen, Waltham, MA); the latter encodes for the Zeocin resistance gene, in which the AOX1 promoter precedes the N-termini and a 6 × His tag follows the C-termini of the C9–HBP genes to be inserted. The digested C9–HBP clones and the pPICZαA vector were then ligated and transformed into *Escherichia coli* electro-competent cells, which were plated on LB agar plates with 50 μg/ml Zeocin (Invitrogen). The plasmid was extracted from several randomly selected colonies and the correct sequence was verified in the Genetics Unit of the National Institute for Biotechnology in the Negev [NIBN; Ben-Gurion University of the Negev (BGU), Israel]. Next, 100 μg of plasmids with the correct sequence were linearized with the restriction enzyme *Sac*I (New England Biolabs) and the digested plasmids, each containing one of the clones (N-TIMP2$_{WT}$, C9, C9–HBP1, C9–HBP2, or C9–HBP3), were transformed into electro-competent X33 *P. pastoris* according to the pPICZα protocol. The transformed yeasts were grown on YPDS plates (2% peptone, 1% yeast extract, 2% D-glucose, 1 M sorbitol, 2% agar) for 72 h at 30 °C, and the expression levels of several colonies from each transformation were then determined. Specifically, four colonies from each protein were taken from the plates, grown overnight at 30 °C in 5 ml BMGY medium [2% peptone, 1% yeast extract, 0.23% $K_2H(PO_4)$, 1.1812% $KH_2(PO_4)$, 1.34% yeast nitrogen base, 4 × 10^{-5}% biotin, 1% glycerol], and then grown for an additional 72 h at 30 °C in a 5 ml inductive BMMY medium [2% peptone, 1% yeast extract, 0.23% $K_2H(PO_4)$, 1.1812% $KH_2(PO_4)$, 1.34% yeast nitrogen base, 4 × 10^{-5}% biotin, 0.5% methanol] with 1% methanol added in 24 h intervals. The cells were then centrifuged, and the supernatant analyzed by western blot to determine the expression levels of the secreted proteins.

For western blot analyses, we used a 1:3000 dilution of a mouse anti-6 × His primary antibody (Abcam, Cambridge, UK), followed by a 1:5000 dilution of an anti-mouse secondary antibody conjugated to alkaline phosphatase (Jackson ImmunoResearch, West Grove, PA) and incubation in 2 ml of a 5-bromo-4-chloro-3-indolyl phosphate reagent (Sigma-Aldrich, Saint Louis, MO). For the large-scale production of the proteins, we chose the yeast that exhibited the highest N-TIMP2$_{WT}$, C9, and C9-HBP1/2/3 protein expression and grew it first in a 50 ml BMGY medium overnight, and then for an additional 72 h in an inductive BMMY medium with daily additions of 1% methanol. On the second and third days of induction, 1 mM phenylmethylsulfonyl fluoride (PMSF; Roche, Basel, Switzerland) and one tablet of cOmplete™ ULTRA Tablets, EDTA-free, Protease Inhibitor Cocktail (Roche) were added to the growth medium (500 ml). The proteins were purified by centrifuging the yeast cell suspension at 4000 g for 30 min, filtering the supernatant, adding 300 mM NaCl, 10 mM imidazole, and 1% glycerol, and titrating with NaOH to pH 8.0. The supernatant was incubated for 1 h at 4 °C, centrifuged for 10 min at 4000 *g*, and filtered. The filtered solution was then loaded onto a HisTrap™ Fast Flow nickel column (Cytiva, Marlborough, MA), washed with two column volumes of 50 mM Tris, pH 7.5, 1 M NaCl, and then washed again with 50 mM Tris, pH 7.5, 300 mM NaCl, 10 mM imidazole, and 5% glycerol. The protein was then eluted with 50 mM Tris, pH 7.5, 300 mM NaCl, and 250 mM imidazole and concentrated using a Vivaspin centrifugal concentrator with a 5-kDa cutoff (Cytiva). The proteins were purified by using a Superdex 75 column with phosphate-buffered saline (PBS) in an ÄKTA pure instrument (Cytiva). An SDS-PAGE of the purified proteins was conducted on a 15% polyacrylamide gel under non-reducing conditions, and the bands were visualized by staining with InstantBlue® Coomassie (Abcam). If needed, the protein samples were concentrated by using a Vivaspin centrifugal concentrator with a 5-kDa cutoff (Cytiva) to reach a final protein concentration of ~1 mg/ml, as determined by UV–Vis absorbance at 280 nm with a NanoDrop Spectrophotometer (Thermo Scientific, Waltham, MA) with an extinction coefficient (ε_{280}) of 13,325 M^{-1} cm^{-1} for C9; 14,815 M^{-1} cm^{-1} for C9–HBP1; 16,305 M^{-1} cm^{-1} for C9–HBP2; 17,795 M^{-1} cm^{-1} for C9–HBP3, and 13,325 M^{-1} cm^{-1} for N-TIMP2$_{WT}$. The production yielded quantities of 0.3–2.0 mg protein per liter for all proteins.

The human MMP-9$_{CAT}$ (residues 107–215 and 391–443) was purified as described previously [45], with the following modifications: The gene was expressed in Bl21(DE3) pLysS *E. coli* cells in a pET28 vector (with an N-terminal 6 × His tag) and induced with 1 mM isopropyl b-D-1-thiogalactopyranoside (IPTG, Sigma-Aldrich) overnight at 30 °C. The cells were then harvested and three rounds of sonication and centrifugation at 12,000 *g* were used to isolate the inclusion bodies, which were then solubilized in 8 M urea and 25 mM Tris, pH 7.5. Next, the enzyme was loaded onto a nickel column and eluted with 8 M urea, 25 mM Tris, pH 7.5, 30 mM NaCl, and 200 mM imidazole. Refolding was conducted by slow dialysis over 3 days at 4 °C with a gradient of urea concentrations, decreasing from 8 M to 0 M. Finally, the enzyme was purified by size exclusion on a Superdex 75 gel-filtration column (Cytiva) with 20 mM Tris, pH 7.5, 50 mM NaCl, and 5 mM $CaCl_2$. The concentration of MMP-9$_{CAT}$ was determined by UV–Vis absorbance at 280 nm, using a NanoDrop Spectrophotometer (Thermo Scientific) with an extinction coefficient (ε_{280}) of 33,920 M-^{1} cm^{-1}. The production yielded ~0.1 mg enzyme per liter, and the purity of the MMP-9$_{CAT}$ was determined by SDS-PAGE.

2.2. MMP-9 $_{CAT}$ inhibition assays

The inhibitory activity of N-TIMP2$_{wt}$, C9, and C9–HBP1/2/3 was evaluated by incubating each of them (0–1.5 nM) with 0.325 nM of purified MMP-9$_{CAT}$ in a TCNB buffer (50 mM Tris, pH 7.5, 100 mM NaCl, 5 mM $CaCl_2$, and 0.05% Brij) at 37 °C for 1 h. The fluorogenic substrate Mca-Pro-Leu-Gly-Leu-Dpa-Ala-Arg-NH2·TFA [where Mca is (7-methoxycoumarin-4-yl) acetyl, Dpa is N-3-(2,4-dinitrophenyl)-*L*-2,3-diaminopropionyl, and TFA is trifluoroacetic acid] (Merck Millipore, Burlington, MA) was added to a final concentration of 7.5 μM. The fluorescence was monitored with 340/30 excitation and 400/30 emission filters by using a Synergy 2 plate reader (BioTek, Winooski, VT) for 60 min at 37 °C. The initial reaction rates at different inhibitor concentrations were determined from the linear increase in fluorescence intensity caused by the cleavage of the fluorogenic substrate. Data were fitted to Morrison's equation (Eq. 1) for tight-binding inhibition by using Prism (GraphPad Software). Ki values were calculated by plotting the initial velocities against the concentrations of the different inhibitors, and they are provided here as averages (± standard deviations, SDs) of three independent experiments. The calculations were performed using a K_M value of 6.175 μM for MMP-9$_{CAT}$, as determined by measuring MMP-9$_{CAT}$ activity against different concentrations (0–50 μM) of the fluorogenic substrate and fitting the data to the Michaelis-Menten equation (Eq. 2), using Prism. The K_M values and their standard errors of the mean (SEMs) are provided as averages obtained from three independent experiments.

$$\frac{V_i}{V_0} = 1 - \frac{([E] + [I] + K_i^{app}) - \sqrt{([E] + [I] + K_i^{app})^2 - 4[E][I]}}{2[E]} \quad (1)$$

where V_i is the enzyme velocity in the presence of the inhibitor; V_0 is the enzyme velocity in the absence of an inhibitor; E, I, and S are the concentrations of the enzyme, inhibitor, and substrate, respectively; K_M is the Michaelis-Menten constant; and Ki^{app} is the apparent inhibition constant, which is given by Eq. 3.

$$V = \frac{V_{max}[S]}{K_M + [S]} \quad (2)$$

where V is enzyme velocity; V_{max} is maximum enzyme velocity, achieved at maximum substrate concentration; S is the substrate concentration; and K_M is the Michaelis-Menten constant.

$$K_i^{app} = K_i\left(1 + \frac{[S]}{K_M}\right) \quad (3)$$

where Ki is the inhibition constant; S is the substrate concentration; and K_M is the Michaelis-Menten constant.

2.3. Gelatinase zymography assay

We determined the ability of N-TIMP2 inhibitors (N-TIMP2$_{WT}$, C9 and C9–HBP1/2/3) to inhibit the gelatinolytic activity of the human recombinant full-length MMP-9 (MMP-9$_{FL}$; Ala20-Asp707; R&D Systems, Minneapolis, MN) on an 8% SDS-PAGE embedded with 1% gelatin (Sigma-Aldrich) [46]. The MMP-9$_{FL}$ was first activated by adding 4-aminophenylmercuric acetate (APMA) to a final concentration of 1 mM and incubating for 24 h at 37 °C [47], and then resolved on SDS-PAGE. Next, the gels were rinsed for 1 h in 2.5% Triton X-100 (Sigma-Aldrich) at room temperature with gentle agitation and incubated overnight at 37 °C in a development buffer (50 mM Tris-HCl, pH 7.5, 10 mM $CaCl_2$, 0.02% NaN_3), either without (control) or with 100 nM of N-TIMP2$_{WT}$, C9, or C9–HBP1/2, or with 2–70 nM for C9–HBP3. Following the incubation, the gels were stained with SimplyBlue™ SafeStain (Thermo Fisher) and the gelatinolytic activity was visualized as clear bands. The signal was quantified by using ImageJ software. The experiment was performed in triplicate and the average and SEM values were determined.

2.4. Surface plasmon resonance binding experiments

The binding affinity between the proteins (C9 and C9–HBP1/2/3) and either AlgS or heparin (1 mg/ml, dissolved in deionized water) was detected by surface plasmon resonance (SPR) spectroscopy, using a ProteOn XPR36 system (Bio-Rad, Hercules, CA). Biotinylated AlgS and heparin were generated as described previously [48] and immobilized [0.5 μg in 150 μl PBS and 0.05% tween (PBST)] using an NLC chip (Bio-Rad) to three channels coated with a NeutrAvidin at a flow rate of 30 μl/min for 5 min; a fourth channel, immobilized with PBST, was used as a control. The proteins were diluted in a mixture of 50 mM Tris, pH 7.5, 300 mM NaCl, and 5 mM $CaCl_2$, and then circulated at a flow rate of 40 μl/min for 613 s, followed by 10 min of dissociation. C9 was diluted to 50, 100, 200, 400, or 800 nM; C9–HBP1 was diluted to 25, 50, 100, 200, or 400 nM; C9–HBP2 was diluted to 1.25, 2.5, 5, 10, or 20 nM when tested for binding to AlgS, and to 6.25, 12.5, 25, 50, or 100 nM when tested for binding to heparin; C9–HBP3 was diluted to 6.25, 12.5, 25, 50, or 100 nM. The binding response, indicated as response units (RU), was determined as a function of time at 25 °C and the equilibrium affinity constants (K_D) between the proteins and AlgS or heparin were determined by using equilibrium-binding analysis. In all cases, the χ^2 values used for the analyses were lower than 10%.

2.5. Particle formation

Alginate was sulfated by the conversion of the sodium salt of the polysaccharide to a tertiary amine salt, followed by *O*-sulfation with carbodiimide (DCC) and sulfuric acid [36]. The sulfated alginate has been previously characterized, both spectrally and biochemically, including by solution ^1H and ^{13}C nuclear magnetic resonance, Fourier-transformed infrared spectroscopy, a scanning electron microscope elemental analysis, and a Sheniger biochemical assay for sulfur quantification [36]. The molecular weights of the raw, heat-treated, and sulfated alginate have also been previously determined by size-exclusion chromatography (SEC). Here, alginate (1% *w/v* in deionized water) was heat-treated to yield low molecular weight fragments of 10 kDa, as determined by SEC coupled to a multiangle laser light scattering photometer (MALLS). The SEC–MALLS indicated that the sulfation reaction resulted in the depolymerization of the alginate molecule, as the average molecular weight of the alginate decreased from 100 to 10 kDa [36].

Prior to particle preparation, AlgS was sterilized by exposing it to UV light (three cycles) and the C9 proteins were centrifuged in a 0.22 μm centrifugal ion-filtration unit (Merck Millipore). The particles were generated by mixing the sterilized AlgS solution (1 mg/ml, dissolved in deionized water) with the various C9–HBP proteins at a 1:2 M ratio, all in a biological hood. To achieve binding equilibrium between the protein and the AlgS, and to allow the particles to form [35], the mixture was vortexed and incubated for 1 h at 37 °C, and was then incubated overnight at 4 °C to stabilize the particles. Before injecting them into the mice, the particles were washed three times with 10 mM HEPES, using a Vivaspin with a 30 kDa cutoff. In some experiments, a mixture of AlgS and C9 (at a 1:2 M ratio) was used as a negative control, as particles cannot form in such a mixture.

2.6. Dynamic light scattering measurements

Dynamic light scattering (DLS) measurements were performed using a Zetasizer Nano-ZS (Malvern Panalytical, Malvern, UK). The samples were dissolved in a buffer (either 50 mM Tris, pH 7.5, 300 mM NaCl, and 5 mM $CaCl_2$ for C9-derived proteins, or 10 mM HEPES for C9–HBP3–AlgS particles) to a final concentration of 0.3 mg/ml (proteins) and 0.18 mg/ml (particles) and equilibrated for 5 min at 25 °C prior to data collection. Correlograms were collected at 173° for at least ten runs of 10 s each. The recorded correlograms were analyzed by using the CONTIN procedure [49,50] with the software provided with the instrument. The sizes and standard distributions of the particles were calculated from the translational diffusion coefficient by using the Stokes-Einstein equation (Eq. 4).

$$d_h = \frac{kT}{3\pi\eta D} \tag{4}$$

where d_h is the hydrodynamic diameter; D is the translational diffusion coefficient; k is Boltzmann's constant; T is the absolute temperature; and η is the viscosity.

2.7. Small-angle X-ray scattering

Small-angle X-ray scattering (SAXS) patterns of the C9, C9–HBP1, and C9–HBP3 protein solutions were recorded at the bio-SAXS BM29 beamline at the European Synchrotron Radiation Facility (ESRF) in Grenoble, France, using an energy of 12.5 keV. The scattering intensity was recorded with a Pilatus3 2 M in-vac detector, with the interval $0.004 < q < 0.5$ Å^{-1}. Ten frames of 2 s exposure time were recorded for each sample. Measurements were performed at either room temperature or at 37 °C in flow mode, where samples were pushed through the capillary at a constant flow rate. The dedicated beamline software was used for data collection and processing. The scattering spectra of the solvent were subtracted from the corresponding solution spectra by using the Irena package for the analysis of small-angle scattering data [51]. The concentration of the three studied proteins was 1 mg/ml (58.35 μM, 53.90 μM, and 46.77 μM for C9, C9–HBP1, and C9–HBP3, respectively), while the concentrations of the samples of mixed protein and AlgS (MW = 10 kDa) were 0.74 mg/ml protein (43.18 μM, 39.89 μM, and 34.62 μM for C9, C9–HBP1, and C9–HBP3, respectively) and 0.18 mg/ml AlgS (18 μM). The size of the proteins was evaluated by using the Guinier approximation [49,52] (Eq. 5).

$$I(q) = I(0)exp\left(\frac{-q^2R_g^2}{3}\right) \tag{5}$$

where I is the intensity; q is the scattering vector; and R_g is the radius of gyration.

2.8. Cryo-transmission electron microscopy

Cryo-transmission electron microscopy (cryo-TEM) was used to image the solutions and dispersions directly. Vitrified specimens were prepared on a copper grid coated with a perforated lacy carbon 300 mesh (Ted Pella Inc., Redding, CA), and a drop of the solution (typically 3 μl) was applied to the grid, blotted with a filter paper to form a thin liquid film, and immediately plunged into liquid ethane at its freezing point (−183 °C). The procedure was performed automatically in the EM GP Plunger (Leica microsystems, Wetzlar, Germany). The vitrified specimens were transferred into liquid nitrogen for storage and then studied using an FEI Talos F200C TEM (200 kV, −180 °C). To minimize electron beam radiation damage, the images were recorded on a slow-scan cooled CCD at low-dose conditions.

2.9. In vitro sustained release studies

The experiments were conducted at four time points ($t = 0$, 2, 4, and 6 days), for both C9–HBP1–AlgS particles and C9–HBP3–AlgS particles (120 μl sample in each case). The samples were centrifuged at top speed (21,380 g) for 1 h at 4 °C and the supernatant (100 μl) was discarded. The pellet containing the precipitated C9–HBP1–AlgS or C9–HBP3–AlgS particles was collected and stored at −80 °C until the end of the analysis. The pellets from the other tubes were re-suspended in 100 μl of fresh PBS (to simulate the body conditions in which the released protein is cleared from the surroundings of the particles) and incubated at 37 °C until the next time point. After 6 days, the pellets were analyzed by western blot, using a 1:3000 dilution of mouse anti-6 × His primary antibody (Abcam) followed by a 1:2000 dilution of anti-mouse secondary antibody conjugated to HRP (Cell Signaling Technology, Danvers, MA), with detection *via* chemiluminescence (EZ-ECL, Biological Industries, Beit Haemek, Israel) and signal quantification with ImageJ software. Each experiment was performed in triplicate and the average and SEM values were determined.

2.10. Thermal stability analysis

C9 and C9–HBP3 (20 μM in 100 μl PBS) were scanned at 210 nm to monitor changes in ellipticity as a function of temperature. Each sample was scanned in the temperature range of 25–90 °C with 5 °C intervals. CD spectra were recorded using a Jasco J-815 spectropolarimeter (Jasco, Japan) equipped with a PTC-348WI temperature controller. A PBS baseline was measured and subtracted from all samples. The data were normalized according to Eq. 6.

$$\theta\left(deg \times cm^2 \times dmol^{-1}\right) = \frac{Ellipticity(\mathrm{mdeg}) \times 10^6}{Pathlength(mm) \times [Protein](\mu M) \times n} \quad (6)$$

where ellipticity is the raw data from the instrument, n is the number of peptide bonds (153 and 196 bonds for C9 and C9–HBP3, respectively), and the cuvette path length was determined as 1 mm.

2.11. In vivo studies

All animal experiments were conducted according to protocols approved by the Committee of Use and Care of Animals at BGU (permits IL-10-02-2019D and IL-29-06-2020C), and they were performed on 10–12 w-old female Balb/C mice. The mice were obtained from Envigo Laboratories (Jerusalem, Israel) and kept under standardized conditions throughout the study, including a 12:12 h light:dark cycle, 20–24 °C, and 30–70% relative humidity. The mice were free-fed autoclaved rodent chow and had free access to water. All the mice were monitored daily for signs of stress or excessive weight loss, according to guidance from the BGU veterinary services [assured by the Office of Laboratory Animal Welfare (OWLA) no. A5060–01 and fully accredited by the Association for Assessment and Accreditation of Laboratory Animal Care International (AAALAC)]. At the end of each experiment, the mice were euthanized under deep anesthesia.

2.12. In vivo sustained release study: Hip-muscle injection

The C9, C9–HBP1, and C9–HBP3 proteins were labeled with Alexa fluor 680 (Thermo Fisher) at 1:2 M ratios according to the manufacturer's instructions, and particles composed of AlgS and each of the labeled proteins were generated as described above. Altogether, four types of samples were injected into the hip muscle of 12-w-old mice: C9–HBP3; a mixture of C9 and AlgS; C9–HBP1–AlgS particles; and C9–HBP3–AlgS particles. Prior to the injection, the fluorescence of the samples was measured with an *in vivo* imaging system (IVIS, Xenogen Corporation, Alameda, CA) and all the samples were diluted to reach the same fluorescence signal. The leg of the mouse was shaved and the samples were then injected into the hip muscle at five different positions (10 μl in each injection, 50 μl total). The fluorescence signal was measured in the live mice over time by using IVIS. At the end of the experiment, the mice were sacrificed, their internal organs and legs were removed, and the fluorescence signal was measured in the legs, heart, liver, lungs, and kidneys. Results are shown as the average (± SEM) of either three or four measurements.

2.13. In vivo sustained release study: Left-ventricular myocardial injection

The C9–HBP1 and C9–HBP3 proteins were labeled and mixed with AlgS as described above. Before injecting the particles into the LV myocardium of female mice, the fluorescence of the particle solutions was measured with NEWTON 7.0 (Vilber, Lourmat, France) and the C9–HBP1–AlgS solution was diluted to reach the same fluorescence as the C9–HBP3–AlgS solution. Then, the chest and abdomen were shaved and the mice were anesthetized with isoflurane, intubated, ventilated, and placed on an isothermal pad. The chest was surgically opened under sterile conditions at the 3rd left intercostal space and the pericardium was exposed. The intramyocardial injections were performed with a 33 G needle connected by a flexible polyurethane tube to a Stepper™ pipette (Dymax, Torrington, CT) that enables multiple fixed-dose injections. We performed five standard 10 μL injections (50 μl total) of either C9–HBP3–AlgS or C9–HBP1–AlgS (as a reference) near the LV apex (one injection), in the middle of the LV (two injections), and near the LV base (two injections). In each injection, the needle was inserted ~1 mm into the tissue and the solution was injected. After 10 s, the needle was extracted and moved to the next location. Following this procedure, air was expelled from the chest by gentle compression before rapidly closing the incision with Histoacryl® (B. Braun, Melsungen, Germany). A buprenorphine injection (0.1 mg/kg, subcutaneously, twice a day) was used for post-surgical analgesia in the first 48 h and dipyrone (1.25 mg/ml) was added to the drinking water of the mice throughout post-operative days 1–3. After they had recovered from the anesthesia, the mice were returned to their cages and they were sacrificed at different time points following the injection ($t = 0$ h, $t = 5$ h, $t =$ 24 h, t = 2 days, and $t = 6$ days). Then, the hearts were removed, and the fluorescence intensity of the labeled proteins was measured with NEWTON 7.0, quantified, and analyzed with Prism (GraphPad Software). Results are reported as the means (± SEM) of either three or four measurements.

2.14. MI experiments: Myocardial C9–HBP3–AlgS injection

The mice went through a left thoracotomy under an isoflurane anesthesia, as described above. To induce MI, the left anterior descending (LAD) coronary artery was permanently ligated by using a 7–0 polyethylene suture. Immediately after the MI induction, 50 μl of either C9–HBP3–AlgS, C9–-HBP3–AlgS×5 or HEPES (10 mM, as a control) was injected into the heart in five 10 μl doses, and air was expelled

from the chest by a gentle compression before closing the incision with Histoacryl® (B. Braun). Post-operative recovery and analgesia were performed as detailed above.

2.15. MI experiments: Heart function assessment

On days 4 and 28 following the MI induction procedure, the chest was re-shaved, and the mice were anesthetized with isoflurane (3% for induction and 1.5% for maintenance, in 100% O_2) and placed supine on an isothermal heating pad. Echocardiograms were performed with a Vevo® 3100 system (VisualSonics, Toronto, Canada) and the time of the procedure was restricted to <15 min to prevent bradycardia (*i.e.*, heart rate < 400 bpm). The heart was imaged in the 2D mode in the parasternal long- and short-axis views of the LV. M-mode images were obtained at the level of the papillary muscles. The LV ejection fraction (EF), which measures the percentage of blood leaving the heart each time it contracts, was calculated as follows:

$$EF\% = \left[\frac{LVEDV - LVESV}{LVEDV}\right] x100$$

where LVEDV and LVESV are the left-ventricular end-diastolic and -systolic volumes, respectively.

During the examination, special care was taken to avoid excessive pressure on the mice. All measurements were averaged for three consecutive cardiac cycles and performed by an experienced technician blinded to the experimental conditions. All surviving mice went through the full analysis, but only mice whose %EF was ≤40% in the initial echocardiography were considered as positive for significant MI and used for further analyses.

2.16. MI experiments: Histological and morphometric analyses

After the final echocardiography, the hearts of the mice were extracted under deep pentobarbital anesthesia. The mice were injected i.p. with heparin (1 unit/g), the thoracic cavity was opened, and the beating heart was quickly removed into a cold 1 M KCl solution (to obtain muscle relation). The hearts were washed and cleaned with PBS, fixed in 4% formaldehyde (FA; 48 h, 4 °C), and kept in 1% FA (4% FA diluted with PBS) at 4 °C until the histological and morphometric analyses.

After the fixation, the hearts were cut in the short axis plane into three pieces (base, middle, and apex), embedded in paraffin blocks, and sectioned into 5 μm slices (Patho-lab diagnostics, Ness Ziona, Israel). The slides were then deparaffinized in xylene (6 min × 3 cycles), rehydrated (a 100–70% ethanol series), and washed under running purified tap water for 2 min. Next, the slides were placed in a 0.1% (*w/v*) Picro-Sirius Red solution [0.5 g Sirius Red ("Direct Red 80", 365,548, Sigma-Aldrich-Merck) in 500 ml picric acid] for 1 h at room temperature, and the solution was changed twice (each change included three quick dips) with 0.5% (*v/v*) acidified water (2.5 ml acetic acid in 500 ml DDW). Finally, the slides were dehydrated by three quick changes in 100% ethanol, cleared in xylene, and a cover slip was glued onto the slides by using a xylene-based glue. The stained sections were scanned with Pannoramic MIDI II (3DHISTECH, Budapest, Hungary) and the morphological analyses were performed with Caseviewer software (3DHISTECH). The following parameters were measured: average septum thickness [mm] (three measurements in each heart), average scar thickness [mm] (three measurements in each heart), LV cavity area [mm^2], and whole LV area [mm^2]. The relative scar thickness was calculated as the average scar thickness divided by the average wall thickness. The expansion index was calculated as follows:

$$Expansion\ Index = \frac{\left[\frac{LV\ cavity\ area}{Whole\ LV\ area}\right]}{Relative\ scar\ thickness}$$

Fibrosis (namely, collagen content, measured as the percent of collagen in the remote zone) was assessed by using QuPath software [53].

2.17. Statistical analyses

All statistical analyses were performed by using GraphPad Prism version 6.01 for Windows (GraphPad Software). All experimental results are reported as means ± SD or SEM, as indicated, and the number of repetitions for each experiment is noted in the figure captions. A one-way ANOVA was used to compare parameters between experimental groups and a two-way ANOVA was used to compare the changes in echocardiographic measurements between days 4 and 28 in each group and to compare between the amount of each protein released from the particles (*in vitro*) on each day (see the SI section). In the *in vivo* functional experiments, outliers were excluded by using the ROUT method, resulting in the exclusion of three mice from the control group in the analysis of relative scar thickness and of one mouse from the C9–HBP3–AlgS×5-treated group in the analyses of remote fibrosis and expansion index.

3. Results and discussion

3.1. N-TIMP2$_{WT}$ and its variants inhibit MMP-9$_{CAT}$ in vitro

The purification process of N-TIMP2$_{WT}$ and its variants (C9 and C9–HBP1/2/3) is shown in Fig. S1. Inhibition assays (Fig. 1A–E) revealed that the Ki of all variants is in the picomolar range and that all variants inhibit MMP-9$_{CAT}$ to a greater extent than did N-TIMP2$_{WT}$ (Table S1). The fusion of C9 to the HBPs decreased the inhibitory activity of C9 to a relatively small extent, but it was still markedly more potent than N-TIMP2$_{WT}$.

3.2. C9–HBP3 reduces MMP-9 gelatinase activity

MMP-9, also known as gelatinase B [54], demonstrates gelatinolytic activity that can be easily detected as bright bands on a stained gelatin SDS-PAGE (Fig. 1F, G). Therefore, we used a gelatin zymography assay to test the ability of N-TIMP2$_{WT}$ and three of its variants, C9 and C9–HBP1/3, to inhibit the gelatinolytic activity of the recombinant full-length MMP-9 (MMP-9$_{FL}$). All three variants inhibited the activity of MMP-9$_{FL}$ (ranging from a 32% inhibition by C9 to a 96% inhibition by C9–HBP3) to a greater extent than did N-TIMP2$_{WT}$ (Fig. 1H); the most pronounced inhibition was of C9–HBP3, which also demonstrated a dose-dependent inhibition (Fig. 1I). Notably, the Ki of C9–HBP3 for MMP-9$_{CAT}$ was higher than those of C9 and C9–HBP1 (Table S1), such that its MMP-9$_{FL}$-inhibitory activity could be expected to be lower—rather than higher—than that of the two other variants. The fact that C9–HBP3 demonstrated the most pronounced inhibition of MMP-9$_{FL}$ can be attributed to the known ability of the positively charged HBP repeats to tight-bind gelatin B, which is negatively charged in physiological pH [9,55–58].

3.3. Fusing HBP repeats to C9 enhances its binding affinity to AlgS

We used SPR to measure the equilibrium affinity constants (K_D) between AlgS and C9, either fused or unfused to HBP repeats (Fig. 2 and Fig. S2A). Adding more HBP repeats to C9 improved the affinity to AlgS (Table S2), with AlgS-binding K_D values of 1040 ± 64 nM, 182 ± 3 nM, 31 ± 4 nM, and 20 ± 1 nM for C9, C9–HBP1, C9–HBP2, and C9–HBP3, respectively. The SPR sensograms revealed that this improvement in affinity was a result of faster association and slower dissociation rates than C9 by itself.

Another advantage of adding HBP repeats to a therapeutic protein (in this case, C9), beyond improving its ability to bind AlgS, is that the added repeats are positively charged and can interact with other,

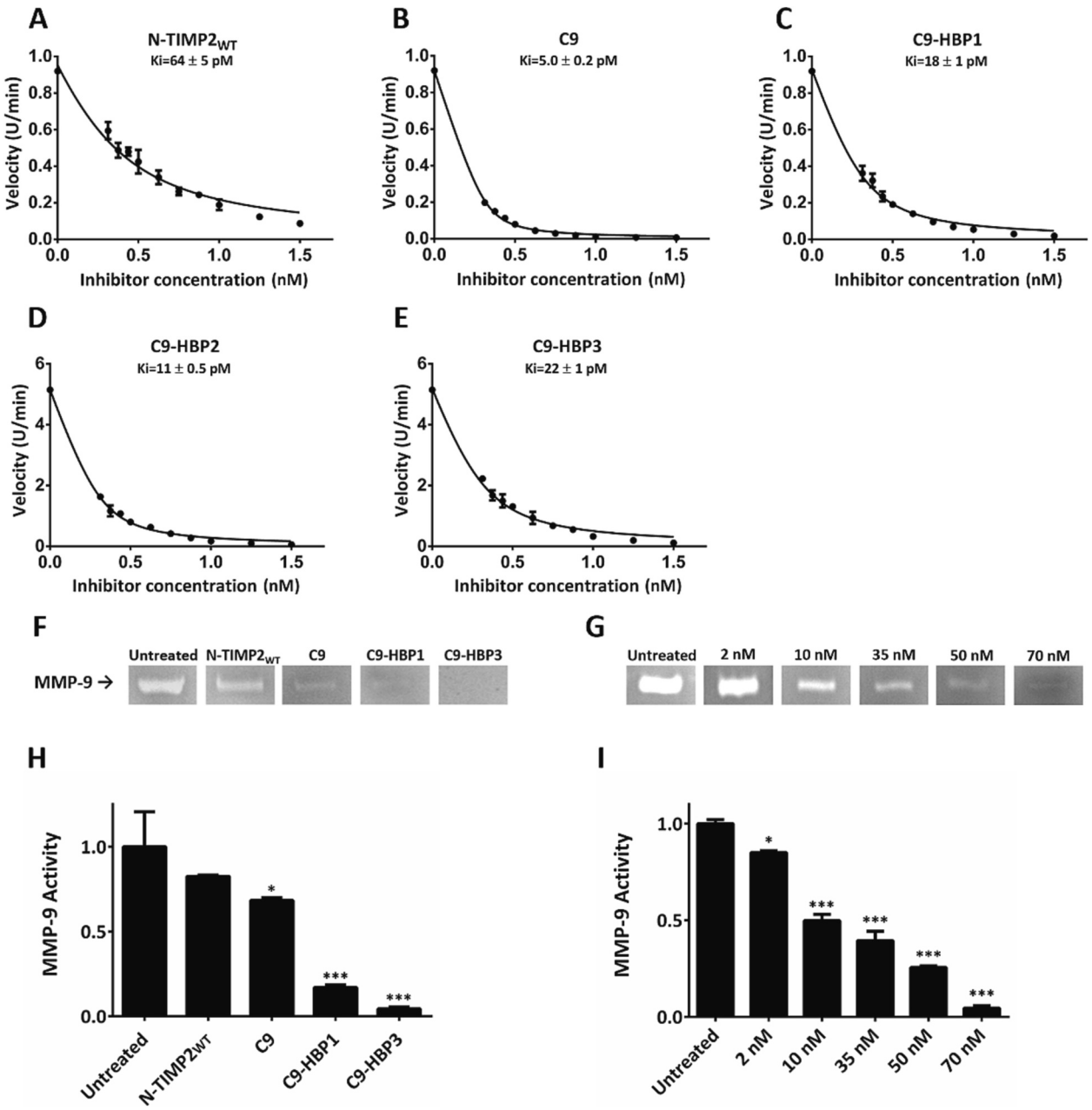

Fig. 1. N-TIMP2 variants inhibit MMP-9 activity *in vitro*. (A–E) Inhibition assays (tight-binding curves). The ability of various concentrations (0.3125–1.5 nM) of N-TIMP2$_{WT}$ (A), C9 (B), C9–HBP1 (C), C9–HBP2 (D), or C9–HBP3 (E) to inhibit the breakdown of a fluorogenic substrate by MMP-9$_{CAT}$ was measured. The cleavage velocity slopes were then calculated and the curves were fitted by the Morrison tight-binding equation (Eq. 1) to extract the inhibition coefficient (Ki). Error bars indicate the standard deviation (SD), $n = 3$. (F—I) Gelatin zymography assays. The inhibition of the gelatinolytic activity of MMP-9$_{FL}$ was measured by adding 100 nM of inhibitor (F, H) or various concentrations of C9–HBP3 (G, I) to a gelatin SDS-PAGE. Panels (H) and (I) quantify the band intensities shown in (F) and (G), respectively, normalized to the intensity of the control (untreated) gel. *$p < 0.05$, ***$p < 0.0001$ (one-way ANOVA followed by Dunnett's multiple comparisons test against the untreated control). Error bars indicate SD, n = 3.

negatively charged components in the tissue, such as heparin/heparan sulfate [36], laminin [59], cellular syndecans, and other glycosaminoglycans [39,40]. This ability facilitates the interaction between the therapeutic protein and the ECM, which is expected to retain the protein locally for longer durations after its release from the particles, prevent its rapid clearance, and increase the overall treatment efficacy. Indeed, our SPR measurements demonstrate that C9–HBP3 binds heparin—a natural component of the ECM—better than C9, C9–HBP1, or C9–HBP2 (Fig. S2B, Fig. S3 and Table S3).

3.4. The effects of HBP fusion on protein nanostructure and thermal stability

To examine the effect of fusing HBP repeats to C9 on the nanostructure and thermal stability of the C9–HBP fusions, we used DLS, SAXS, and cryo-TEM. The DLS profiles (Fig. 3A) reveal that adding HBP repeats to C9 gradually increases the hydrodynamic diameter (d_h) of the protein, indicating an increase in the overall size relative to C9 alone, from 5.2 ± 0.4 nm in C9 to 8.6 ± 0.6 in C9–HBP3 (see Eq. 4). The SAXS profiles of C9, C9–HBP1, and C9–HBP3 (Fig. 3B) exhibit a scattering profile typical of globular structures. The Kratky plots of C9, C9–HBP1, and C9–HBP3 (Fig. 3C) indicate that adding HBP repeats to C9 had a

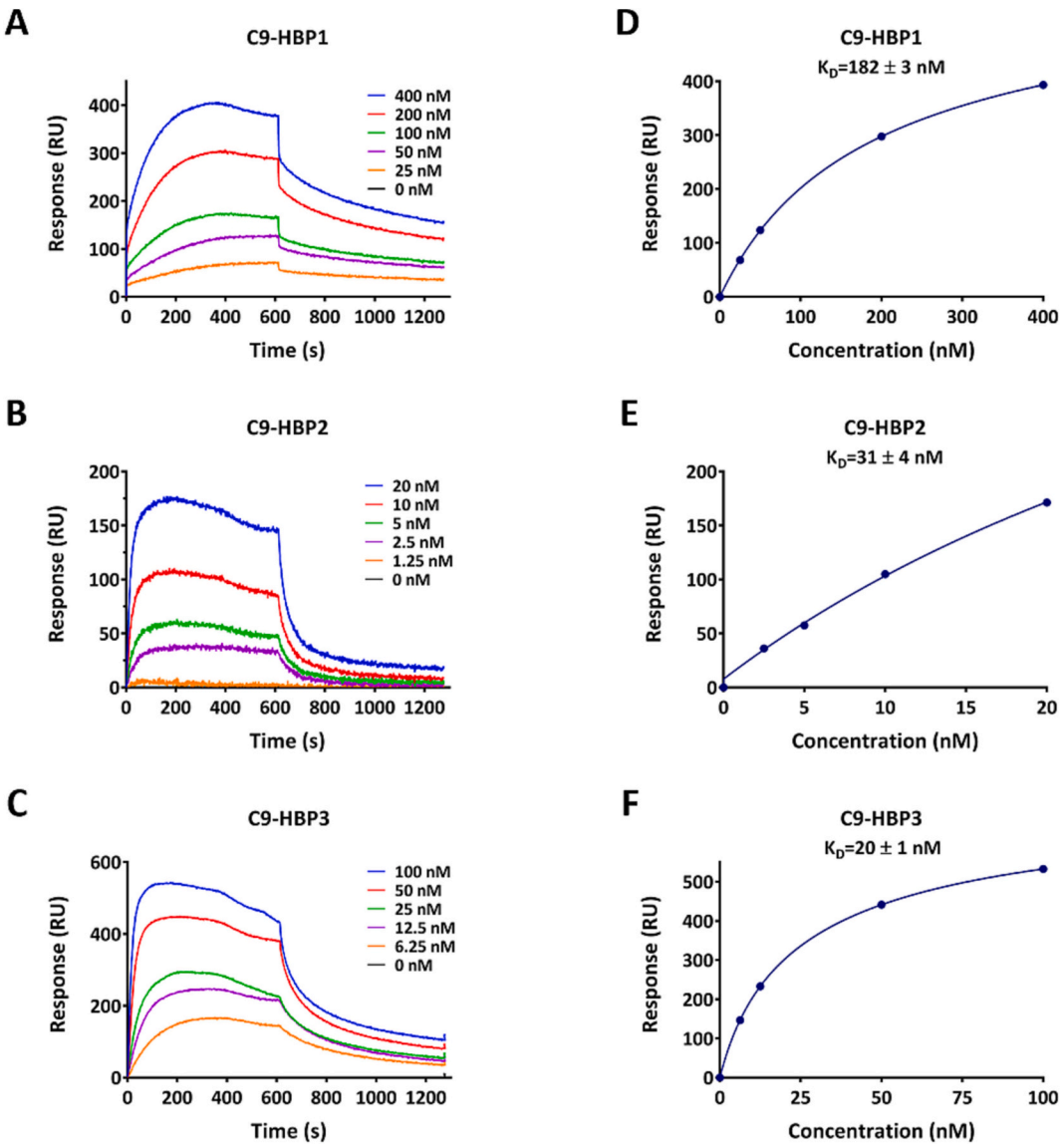

Fig. 2. HBP repeats increase the affinity of C9 to AlgS. SPR measurement results showing the binding to AlgS (A–C; different colors indicate different protein concentrations) and equilibrium analyses (D—F) of C9–HBP1 (A, D), C9–HBP2 (B, E), and C9–HBP3 (C, F).

negligible effect on the folding state of C9, which remained roughly globular [60]. A Guinier approximation (Eq. 5 [52]) revealed that the radius of gyration (R_g) of C9, C9–HBP1, and C9–HBP3 is ~2.1 nm, 2.5 nm, and 2.8 nm, respectively (Fig. S4A). Notably, since R_g (as opposed to d_h) does not include the hydrodynamic shell of the protein [61–63], these findings are in line with the DLS results, although the diameter (calculated from the R_g values) appears to be smaller. Cryo-TEM images, which were obtained only for C9–HBP3 (because the other proteins were too small to be detected) confirm the SAXS results and indicate a spherical structure with an average diameter of 11.26 ± 0.35 nm (Fig. 3D). Increasing the temperature of C9–HBP3 from 25 °C to 37 °C did not affect its SAXS scattering profile (Fig. S4B), indicating that its structure is preserved under relevant body temperatures and highlighting its therapeutic potential.

3.5. C9–HBP–AlgS complexes are assembled into large particles

To be used as a controlled-release system, the C9–HBP–AlgS complexes need to assemble into particles in which the bound and unbound states of the C9–HBP and AlgS are in equilibrium, which would enable the continuous dissociation of C9–HBP from the complex [35] (Fig. S5A). Such an equilibrium depends on the binding affinity (K_D) values of the C9–HBP proteins to AlgS (Fig. 2), which dictate the assembly of the complexes within the particles and, consequently, their structure and size. To ensure the assembly of C9–HBP and AlgS into large particles, we used cryo-TEM. Indeed, a qualitative analysis of the TEM images shows that in the absence of C9–HBP proteins, both AlgS alone (Fig. 3E) and AlgS with C9 (Fig. 3F) show two distinct populations: globular, 300–500 nm aggregates; and dispersed chains, which are likely of unbound AlgS (Fig. 3E, F, inset). Conversely, C9–HBP–AlgS particles (Fig. 3G-I) show a single population of large, micrometer-size aggregates, whose size increases with the addition of HBP repeats, reaching 4.095 ± 0.617 μm in C9–HBP1–AlgS particles (Fig. 3G) and 5.285 ± 0.523 μm in C9–HBP3–AlgS particles (Fig. 3I). A DLS confirmed a size of 5.0 ± 0.5 μm for C9–HBP3–AlgS particles (Fig. S5B). These findings have several implications for the use of C9–HBP–AlgS particles as a controlled-release system. First, since larger particles have a lower diffusion constant [64], particles with more HBP repeats will remain closer to the injection site, thereby increasing the local concentration of the therapeutic protein. Second, the size of the particles is dictated by

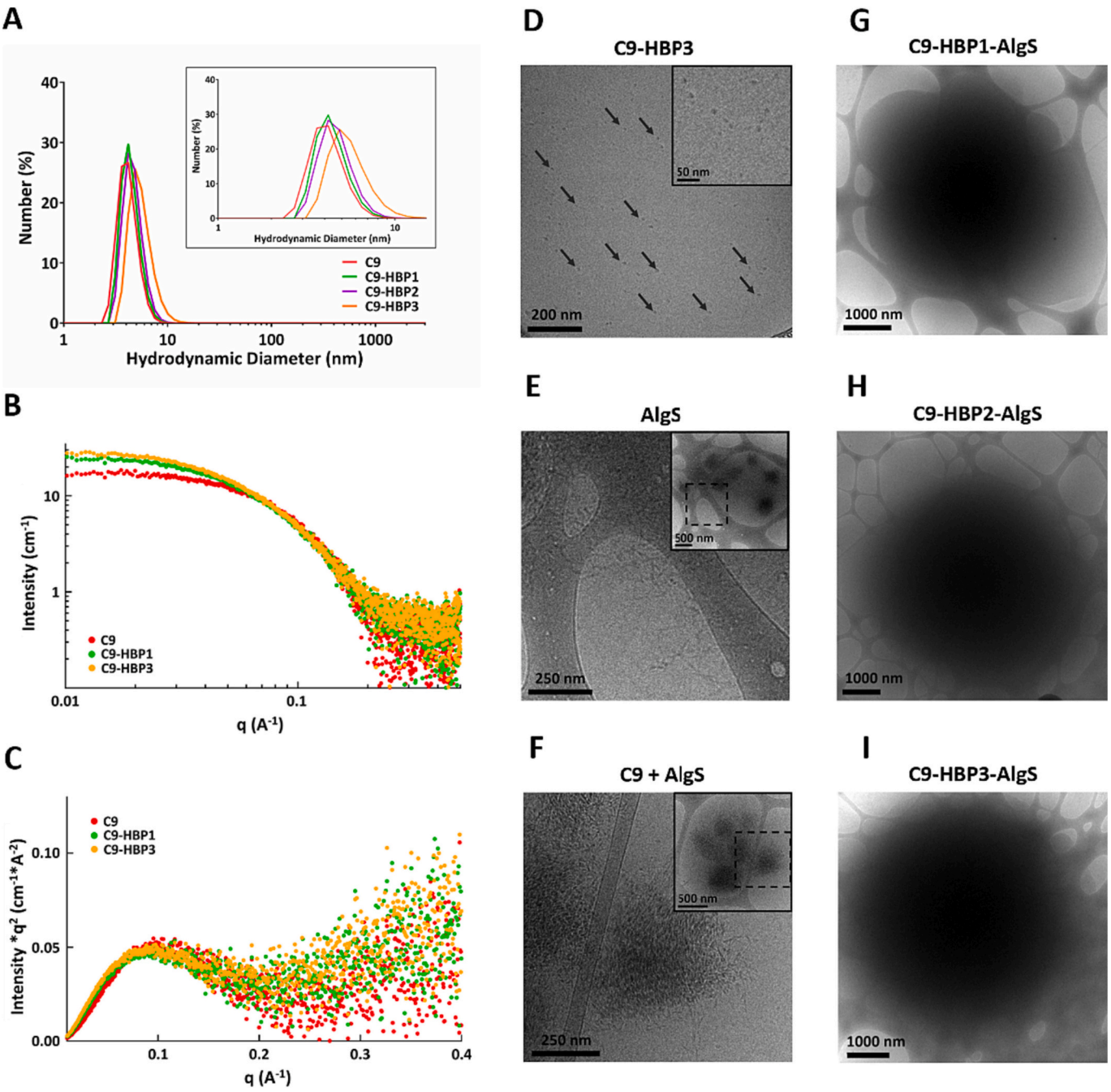

Fig. 3. The structure and assembly of C9 proteins. (A) DLS profiles (particle size distribution) of C9 and C9–HBP1/2/3, overlaid. Inset: a zoomed-in view (d_h of 1–15 nm). (B, C) SAXS profiles in log-log (B) and a Kratky representation (C) of 1 mg/ml C9, C9–HBP1, and C9–HBP3 (58.24 μM, 53.90 μM, and 46.78 μM, respectively) in a Tris buffer (pH 7.5). (D—I) Cryo-TEM images of C9–HBP3 (D), AlgS alone (E), a mixture of C9 and AlgS (F), C9–HBP1–AlgS (G), C9–HBP2–AlgS (H), and C9–HBP3–AlgS (I). Note the increase in particle size with increasing HBP repeats. The arrows in D indicate visible C9–HBP3 molecules.

the strength of the interactions between the bound protein and the biomaterial and by the valency (*i.e.*, avidity) of the HBP repeats, which also dictate the release rate of the protein [65]. Therefore, larger particles with more HBP repeats have stronger protein–biomaterial interactions, which will confer a slower protein release. Third, since the size of the particle is inversely correlated with its surface area-to-volume ratio, particles with more HBP repeats will show a lower release rate [66]. Therefore, changing the number of HBP repeats in the particles can be used as a means to control various aspects of the proposed sustained-release system.

3.6. AlgS prolongs the retention of C9–HBP3 in the tissue in vivo

While proteins with relatively low molecular weights (below 80 KDa) are cleared from the tissue within hours after injection [2], larger particles are retained for longer durations [67,68]. To test whether interacting C9–HBP3 with AlgS can facilitate retention in the tissue for therapeutically relevant durations, we injected either C9–HBP3 or particles of C9–HBP3–AlgS, both fluorescently labeled with Alexa fluor 680 and diluted to reach the same fluorescence level (Fig. S6), directly into the hip muscles of mice, and then monitored the fluorescent signal over time (Fig. 4A). The signal of C9–HBP3 began to decay 2–3 min after the

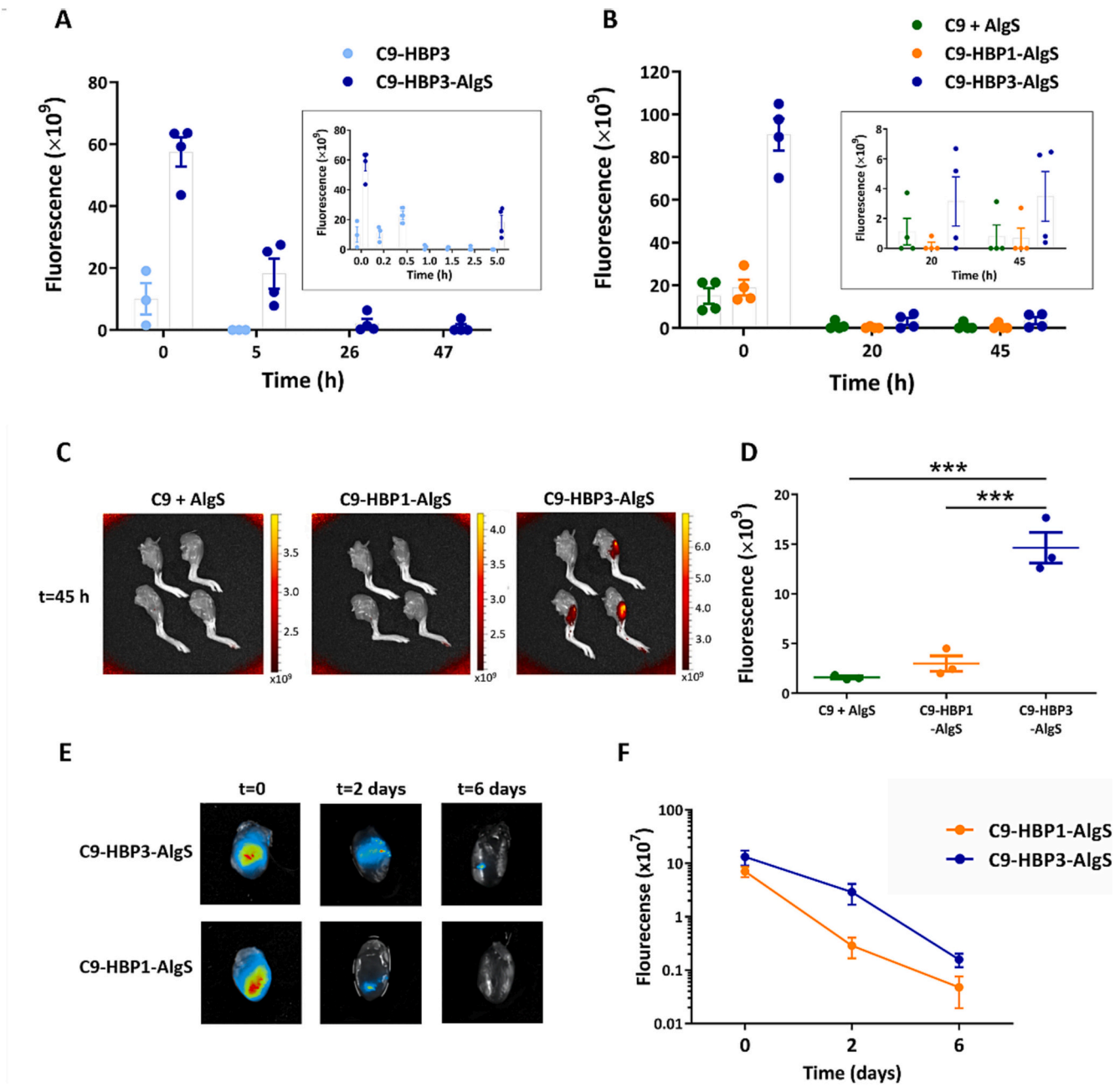

Fig. 4. AlgS and HBP repeats sustain C9 release *in vivo*. C9, C9–HBP1 and C9–HBP3 were fluorescently labeled, injected with or without AlgS into the hip muscle (A–D) or heart (E, F) of mice, and monitored in the living mice using IVIS. (A) Adding C9–HBP3 to AlgS increased the retention time of C9–HBP3 in the tissue. The inset shows the fluorescence intensity in the first 5 h following the injection. (B) HBP repeats increase the retention time of C9 in the tissue. The inset shows the fluorescence intensity at 20 h and 45 h following the injection (note the different y-axis scales). (C) The legs of three of the mice from each group shown in B, excised 45 h following the injection, and of three negative-control mice (top left leg in each image). (D) Quantification of the fluorescence intensity in the excised legs. (E) The fluorescence signal in the heart, detected with NEWTON 7.0 at different time points after a transepicardial injection of C9–HBP1–AlgS or C9–HBP3–AlgS particles into the left ventricular myocardium. (F) Quantification of the fluorescence intensity in the heart of the mice shown in E. In all experiments, the fluorescence signal of a negative-control organ (a leg in A, B, and D, or a heart in F) was subtracted from the signal of the injected mice. Bars represent means ± SEM, $***p < 0.0001$ (one-way ANOVA with Tukey's multiple comparisons post-hoc test), $n = 3$ or 4 in each experiment.

injection ($t = 0$ in Fig. 4A), probably due to its rapid clearance from the injected tissue, and it decayed completely after 1.5 h (Figs. 4A, inset, S7). Conversely, the C9–HBP3–AlgS signal was still detectable in the hip muscles of the living mice 26 h after the injection (Figs. 4A, S8). Next, the mice were sacrificed (21 h or 47 h after the injection with C9–HBP3 and with C9–HBP3–AlgS, respectively) and their legs, hearts, livers, lungs, and kidneys were examined for remaining fluorescent signals. While the signal was still robust in the legs of C9–HBP3–AlgS-injected mice 47 h after the injection (Fig. S8F), it was negligible in the legs of the C9–HBP3-injected mice even after 21 h (Fig. S7F). None of the internal organs in any of the injected mice showed a fluorescent signal (Fig. S9). Taken together, these *in vivo* experiments demonstrate that (a) the formation of a complex between C9–HBP3 and AlgS considerably prolongs the retention of the protein in the injected tissue, and (b) C9–HBP3 does not accumulate elsewhere in the body.

3.7. HBP repeats prolong the protein release from AlgS particles in vivo

How does adding more HBP units affect the rate of protein release from the particles? In an *in vitro* experiment, we tested the sustained release of C9–HBP1 and C9–HBP3 from particles in four time points (0, 2, 4, and 6 days), which reflect those selected for the *in vivo* drug-release experiment (see above; Fig. 4E and F), cover most of the drug-release period, and fit the expression profile of MMP-9, which reaches its highest levels within this period post MI. We found that C9–HBP1 is detectable in the particles 2 days after they were generated, while C9–HBP3 was still detectable, at relatively high levels, 6 days after the particles were generated (Fig. S10). In an *in vivo* study, we fluorescently labeled C9, C9–HBP1, and C9–HBP3 and then injected either a mixture of AlgS and C9 (no particles), C9–HBP1–AlgS particles, or C9–HBP3–AlgS particles into the hip muscles of mice [the solutions were diluted before the injections to reach the same level of fluorescence in all groups (Fig. S11)]. In mice injected with C9–HBP3–AlgS particles, the fluorescent signal was considerably higher a few minutes following the injection (Fig. 4B, t = 0), and it remained detectable for markedly longer (Fig. 4B, inset, S12) than in mice from the other two groups. After sacrificing the mice (45 h post-injection), the signal in the excised hips was significantly more robust in mice injected with C9–HBP3–AlgS particles than in those from the other two groups, in which it was almost undetectable (Fig. 4C, D). No fluorescent signal was detected in the hearts, livers, lungs, or kidneys of mice from any of the three groups (Fig. S13). Finally, in another set of experiments, fluorescently labeled C9–HBP1–AlgS or C9–HBP3–AlgS particles were injected into the myocardium of the LV after diluting the two solutions to reach the same level of fluorescence (Fig. S14). While the initial fluorescence signal (measured 2–3 min following the injection) was similar in both groups, it decayed more slowly and was retained in the tissue for a longer duration (6 days) in mice injected with C9–HBP3–AlgS than in those injected with C9–HBP1–AlgS (Figs. 4E,F, S15). Importantly, the most detrimental effects of MMP-9 in the myocardium take place 2–4 days post-MI [21], during which the inhibitory activity of C9 would be most therapeutically efficient.

Of note, we were unable to fully determine the exact release mechanism of the drug because it depends both on the affinity of the drug to the AlgS particles and on the quantity of the drug that is in complex with the AlgS, relative to the free drug; while we accurately determined the former with SPR, we were unable to accurately determine the latter.

3.8. Treating mice with C9–HBP3–AlgS particles inhibits post-MI remodeling

To evaluate the therapeutic potential of our novel sustained-release system (and, specifically, of the best-performing complex, C9–HBP3–AlgS), and as a proof-of-concept in the context of post-MI treatment, we first confirmed that the inhibitory activity of C9–HBP3 is retained during the time in which the inhibitory activity of C9 in the heart is most needed, *i.e.*, 2–4 days post-MI, when MMP-9 expression levels are highest [21]. Indeed, 4 days after incubation at 37 °C (Fig. S16A, B), C9–HBP3 considerably inhibited MMP-9_{CAT} activity *in vitro,* with Ki values (calculated by using Eq. 1) of 17.9 ± 1.5 pM and 13.6 ± 0.5 pM at $t = 0$ and $t = 4$ days, respectively. The thermal stability of the protein was also confirmed by melting experiment in CD (Fig. S16C). Next, we tested the efficacy of the system in mice in which extensive MI was induced by permanent ligation of the LAD coronary artery. The treatment solution (see below) was injected into the LV myocardium immediately following the LAD ligation *via* five standard injections (10 μl each) of either 10 μg C9–HBP3–AlgS, 50 μg C9–HBP3–AlgS (designated C9–HBP3–AlgS×5), or HEPES only (control). After 4 days and 28 days, echocardiography was performed to assess the ejection fraction (%EF) of the LV, which is indicative of the cardiac systolic function. Other standard functional parameters were also evaluated (Fig. S17 A–F). Notably, as the long-term post-MI remodeling is relevant mainly in the setting of large infarcts [10], we included in our analysis only mice whose initial EF was ≤40%, which is indicative of extensive MI. The initial (4 days) EF of all mice in all groups were not statistically different from one another (Fig. S18).

The initial %EF of the mice that met the inclusion criteria (%EF ≤ 40) was similar in all groups. However, on day 28 post-MI, the %EF was significantly higher in the group treated with C9–HBP3–AlgS×5, reflecting a better systolic function relative to the control group (Fig. 5A). In addition, the average change in %EF between days 4 and 28 post-MI (Fig. 5B) increased in both treated groups, but a statistically significant difference from control was found only for the group treated with C9–HBP3–AlgS×5. Since a more severe MI increases the risk of myocardial remodeling and results in a poorer prognosis [69,70], we further divided each experimental group into two sub-groups: moderate MI (initial %EF ≥ 30) and severe MI (initial %EF < 30). This analysis revealed that the greatest improvement in cardiac function was in mice with severe MI who were treated with C9–HBP3–AlgS×5 (Fig. 5C). It was previously found that patients with severe cardiac dysfunction show an increased ratio of MMP/TIMP expression levels and persistently elevated MMP-9 levels [21,71,72]. These findings are consistent with our current results, which showed increased treatment efficiency in mice with severe MI, and they highlight the specificity of C9–HBP3 as a potent inhibitor of MMP-9-mediated LV remodeling post extensive MI. Histological analyses (Fig. 5D, E) revealed that the percent of fibrosis in the remote area of the heart was significantly lower in mice treated with C9–HBP3–AlgS×5 than in mice treated with C9–HBP3–AlgS, albeit the percent of fibrosis in the two treated groups was not significantly different from that in control mice. In agreement with these findings, morphometric measurements showed that both treatments prevented the thickening of the LV wall in the post-MI scar area (Fig. 5F) and reduced the expansion of the heart (Fig. 5G). Taken together, these experiments show that the timely inhibition of MMP-9 activity by the direct injection of C9–HBP3–AlgS into the heart following MI preserves cardiac function by reducing ECM degradation and subsequent myocardial remodeling.

In our previous work [43], we showed that C9 is highly potent in inhibiting endogenous, cell-secreted MMP-9 in cell that overexpress MMP-9. Notwithstanding, we cannot unequivocally determine that the therapeutic effect shown here—namely, the inhibition of post-MI remodeling—was a result of MMP-9 inhibition alone, rather than of drug interactions with other molecules or MMPs.

4. Conclusions

We describe a novel sustained drug-release system, based on minute spherical particles comprising a therapeutic protein bound to AlgS, and demonstrate its therapeutic applicability. To bind the therapeutic protein to the AlgS, we used 1, 2, or 3 repeats of the heparin-binding protein (HBP), such that the number of repeats directly controls the release rate of the therapeutic protein—a highly desired property in sustained-release systems. As a proof-of-concept, we tested the therapeutic applicability of our system in a case study of post-MI heart remodeling, using the MMP-9 inhibitor protein C9 as a model therapeutic protein. We demonstrate *in vivo* that a direct application of C9–HBP3–AlgS particles into the heart of mice following MI reduces heart remodeling and significantly improves cardiac function, attesting to their sustained and local release within the heart tissue. Notably, although AlgS is biocompatible, over-sulfation may lead to toxic (*e.g.*, anticoagulant) effects [73,74]; such potential toxicity needs to be examined in future studies.

The main advantage of our system is twofold: first, it is universal because it allows the attachment of a wide range of therapeutic proteins to AlgS simply by fusing the short HBP sequence; and second, it is tunable because modifying the number of HBP repeats controls the release rate of the therapeutic protein from the particle. Potentially, this system can be used to apply several types of particles together—each

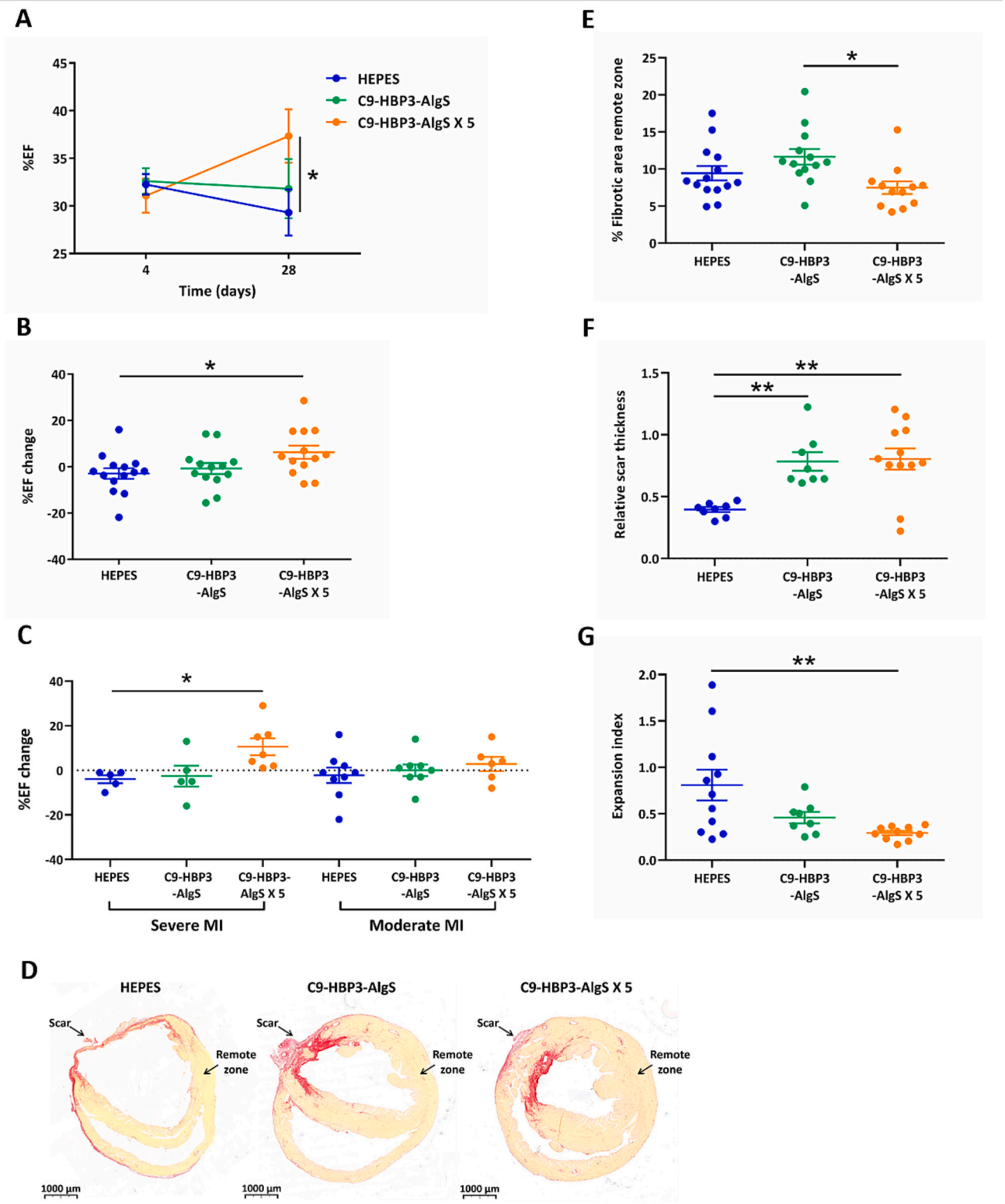

Fig. 5. The therapeutic efficacy of C9–HBP3–AlgS in a mouse model of MI. (A–C) Echocardiogram measurements ($n = 13$ or 14 mice in each group) of (A) the average %EF on days 4 and 28 post-MI; (B) the change in %EF from day 4 to day 28 post-MI; and (C) the change in %EF from day 4 to day 28 in mice with severe *vs.* moderate MI (initial %EF <30 and ≥ 30, respectively). (D–E) Evaluation of post-MI cardiac fibrosis. (D) Representative histological sections of post-MI hearts, stained with Sirius Red to indicate fibrosis; (E) the percentage of fibrosis in the area remote from the MI-induced scar. $n = 12$–14 mice in each group. (F–G) Morphometric measurements of the post-MI heart, including (F) the relative scar thickness, calculated as the thickness of the scar divided by the thickness of the septum ($n = 8$–12 mice in each group); and (G) the heart expansion index (n = 8–11 mice in each group). Bars indicate means ± SEM, $*p < 0.05$ and $**p < 0.01$ [two-way ANOVA with Sidak's multiple comparison test (A); one-way ANOVA with Tukey's multiple comparison test (B, E, F, G); one-way ANOVA with Dunn's multiple comparison test (C)]. (For interpretation of the references to colour in this figure legend, the reader is referred to the web version of this article.)

containing a different therapeutic protein and a different number of HBP repeats—so as to individually adjust the release of each therapeutic protein according to the specific expression profiles of its target.

Ethics approval and consent to participate

All the animal experiments were conducted according to protocols approved by the Committee of Use and Care of Animals at Ben-Gurion University of the Negev [permits IL-10-02-2019D and IL-29-06-2020C].

Consent for publication

All authors agree with the submission, and the work has not been published or submitted for publication elsewhere, either entirely or in part, or in another form or language.

Availability of data and materials

All data generated and analyzed during this study are included in this published article and its supplementary information files.

Competing interests

The authors declare that they have no competing interests.

Funding

This work was supported by the Israel Science Foundation (grant number 1615/19), the Worldwide Cancer Research foundation (grant number 20–0238), and the Israel Cancer Research Fund (ICRF) (grant number 846497) to N.P.

CRediT author statement

Amit Itzhar: Conceptualization, Methodology, Validation, Formal analysis, Investigation, Data curation, Writing — original draft, Writing — review and editing, Visualization. **Gal Yosef**: Conceptualization, Methodology, Validation, Formal analysis, Investigation, Data curation, Writing — review and editing. **Maayan Eilon-Ashkenazy:** Conceptualization, Methodology, Validation, Formal analysis, Investigation, Data curation, Writing — review and editing. **Yulia Shmidov:** Methodology, Validation, Formal analysis, Data curation, Writing — review and editing. **Hadas Gil**: Methodology, Validation, Writing — review and editing. **Sigal Elyagon:** Methodology**,** Formal analysis, Writing — review and editing. **Sharon Etzion:** Validation. **Ronit Bitton:** Validation, Writing — review and editing**. Smadar Cohen:** Conceptualization, Methodology, Validation, Resources, Writing — review and editing, Supervision. **Yoram Etzion:** Conceptualization, Methodology, Validation, Resources, Writing — review and editing, Supervision. **Niv Papo**: Conceptualization, Methodology, Validation, Formal analysis, Investigation, Resources, Writing — original draft, Writing — review and editing, Visualization, Supervision, Project administration, Funding acquisition.

CRediT authorship contribution statement

Amit Itzhar: Writing – review & editing, Writing – original draft, Validation, Methodology, Investigation, Formal analysis, Data curation, Conceptualization. **Gal Yosef:** Writing – review & editing, Validation, Methodology, Investigation, Formal analysis. **Maayan Eilon-Ashkenazy:** Writing – review & editing, Validation, Methodology, Investigation, Formal analysis, Data curation, Conceptualization. **Yulia Shmidov:** Writing – review & editing, Validation, Methodology, Formal analysis, Data curation. **Hadas Gil:** Writing – review & editing, Validation, Methodology. **Shiran Lacham-Hartman:** Data curation, Formal analysis, Investigation, Writing – review & editing. **Sigal Elyagon:** Writing – review & editing, Methodology, Formal analysis. **Sharon Etzion:** Validation. **Ronit Bitton:** Writing – review & editing, Validation. **Smadar Cohen:** Writing – review & editing, Validation, Resources, Methodology, Conceptualization. **Yoram Etzion:** Writing – review & editing, Validation, Supervision, Resources, Methodology, Conceptualization. **Niv Papo:** Writing – review & editing, Writing – original draft, Validation, Resources, Methodology, Investigation, Formal analysis, Conceptualization.

Data availability

The raw data required to reproduce these findings are available to download from SI section. The processed data required to reproduce these findings are available to download from the SI section.

Acknowledgements

The authors thank Dr. Alon Zilka, Dr. Anat Shahar, Dr. Einat Nativ-Roth, and Dr. Petra Pernot for their technical assistance. SPR experiments were performed at the NIBN Proteomics, Cytometry and Microscopy unit.

Appendix A. Supplementary data

Supplementary data to this article can be found online at https://doi.org/10.1016/j.jconrel.2023.10.033.

References

[1] K. Malliaras, E. Marba, Cardiac cell therapy: where we've been, where we are, and where we should be headed, Br. Med. Bull. (2011) 161–185, https://doi.org/10.1093/bmb/ldr018.
[2] E. Ruvinov, J. Leor, S. Cohen, The effects of controlled HGF delivery from an affinity-binding alginate biomaterial on angiogenesis and blood perfusion in a hindlimb ischemia model, Biomaterials 31 (16) (Jun. 2010) 4573–4582, https://doi.org/10.1016/j.biomaterials.2010.02.026.
[3] Z. Fan, et al., Sustained release of a peptide-based matrix Metalloproteinase-2 inhibitor to attenuate adverse cardiac remodeling and improve cardiac function following myocardial infarction, Biomacromolecules 18 (9) (2017) 2820–2829, https://doi.org/10.1021/acs.biomac.7b00760.
[4] B.P. Purcell, et al., Injectable and bioresponsive hydrogels for on-demand matrix metalloproteinase inhibition, Nat. Mater. 13 (March) (2014), https://doi.org/10.1038/NMAT3922.
[5] S.R. Eckhouse, et al., Local hydrogel release of recombinant TIMP-3 attenuates adverse left ventricular remodeling after experimental myocardial infarction, Sci. Transl. Med. 6 (223) (2014), https://doi.org/10.1126/scitranslmed.3007244.
[6] B.P. Purcell, et al., Delivery of a matrix metalloproteinase-responsive hydrogel releasing TIMP-3 after myocardial infarction: effects on left ventricular remodeling, Am. J. Physiol. Heart Circ. Physiol. 315 (4) (2018) H814–H825, https://doi.org/10.1152/ajpheart.00076.2018.
[7] L.L. Wang, J.J. Chung, E.C. Li, S. Uman, P. Atluri, J.A. Burdick, Injectable and protease-degradable hydrogel for siRNA sequestration and triggered delivery to the heart, J. Control. Release 285 (July) (2018) 152–161, https://doi.org/10.1016/j.jconrel.2018.07.004.
[8] S. Chen, et al., An injectable hydrogel to reverse the adverse microenvironment of diabetic infarcted heart, Materialia vol. 15 (November 2020) (2021) 100957, https://doi.org/10.1016/j.mtla.2020.100957.
[9] T. Nii, Strategies using gelatin microparticles for regenerative therapy and drug screening applications, Mol. Rev. (2021) 1–10, https://doi.org/10.3390/molecules26226795.
[10] W.J. Richardson, S.A. Clarke, T. Alexander Quinn, J.W. Holmes, Physiological implications of myocardial scar structure, Compr. Physiol. 5 (4) (2015) 1877–1909, https://doi.org/10.1002/cphy.c140067.
[11] B.C. Berk, K. Fujiwara, S. Lehoux, ECM remodeling in hypertensive heart disease, J. Clin. Invest. 117 (3) (2007) 568, https://doi.org/10.1172/JCI31044.568.
[12] N.G. Frangogiannis, The extracellular matrix in ischemic and nonischemic heart failure, Circ. Res. 125 (1) (2019) 117–146, https://doi.org/10.1161/CIRCRESAHA.119.311148.
[13] D. Curley, B. Lavin Plaza, A.M. Shah, R.M. Botnar, Molecular imaging of cardiac remodelling after myocardial infarction, Basic Res. Cardiol. 113 (2) (2018) 1–18, https://doi.org/10.1007/s00395-018-0668-z.

[14] G.A. Roth, et al., Global, regional, and National Burden of cardiovascular diseases for 10 causes, 1990 to 2015, J. Am. Coll. Cardiol. 70 (1) (2017) 1–25, https://doi.org/10.1016/j.jacc.2017.04.052.
[15] L.G.N. de Almeida, et al., Matrix metalloproteinases: from molecular mechanisms to physiology, pathophysiology, and pharmacology, Pharmacol. Rev. 74 (3) (2022) 712–768, https://doi.org/10.1124/pharmrev.121.000349.
[16] G.V. Halade, Y.-F. Jin, M.L. Lindsey, Matrix metalloproteinase (MMP)-9: a proximal biomarker for cardiac remodeling and a distal biomarker for inflammation, Pharmacol. Ther. 139 (1) (Jul. 2013) 32–40, https://doi.org/10.1016/j.pharmthera.2013.03.009.
[17] M. Lindsey, et al., Matrix-dependent mechanism of neutrophil-mediated release and activation of matrix metalloproteinase 9 in myocardial ischemia/reperfusion, Circulation 103 (17) (2001) 2181–2187, https://doi.org/10.1161/01.CIR.103.17.2181.
[18] R.P. Iyer, M. Jung, M.L. Lindsey, MMP-9 signaling in the left ventricle following myocardial infarction, Am. J. Physiol. Heart Circ. Physiol. 311 (1) (2016) H190–H198, https://doi.org/10.1152/ajpheart.00243.2016.
[19] Y.Y. Li, A.M. Feldman, Y. Sun, C.F. McTiernan, Differential expression of tissue inhibitors of metalloproteinases in the failing human heart, Circulation 98 (17) (1998) 1728–1734, https://doi.org/10.1161/01.CIR.98.17.1728.
[20] M.L. Lindsey, R. Zamilpa, Temporal and spatial expression of matrix metalloproteinases and tissue inhibitors of metalloproteinases following myocardial infarction, Cardiovasc. Ther. 30 (1) (2012) 31–41, https://doi.org/10.1111/j.1755-5922.2010.00207.x.
[21] C.S. Webb, et al., Specific temporal profile of matrix metalloproteinase release occurs in patients after myocardial infarction: relation to left ventricular remodeling, Circulation 114 (10) (2006) 1020–1027, https://doi.org/10.1161/CIRCULATIONAHA.105.600353.
[22] Z. Kassiri, et al., Simultaneous transforming growth factor β-tumor necrosis factor activation and cross-talk cause aberrant remodeling response and myocardial fibrosis in Timp3-deficient heart, J. Biol. Chem. 284 (43) (2009) 29893–29904, https://doi.org/10.1074/jbc.M109.028449.
[23] W.M. Yarbrough, et al., Selective targeting and timing of matrix metalloproteinase inhibition in post-myocardial infarction remodeling, Circulation 108 (14) (2003) 1753–1759, https://doi.org/10.1161/01.CIR.0000091087.78630.79.
[24] R. Mukherjee, et al., Myocardial infarct expansion and matrix metalloproteinase inhibition, Circulation 107 (4) (2003) 618–625, https://doi.org/10.1161/01.CIR.0000046449.36178.00.
[25] A. Ducharme, et al., Targeted deletion of matrix metalloproteinase-9 attenuates left ventricular enlargement and collagen accumulation after experimental myocardial infarction, J. Clin. Invest. 106 (1) (2000) 55–62.
[26] G.A. Cabral-Pacheco, et al., The roles of matrix metalloproteinases and their inhibitors in human diseases, Int. J. Mol. Sci. 21 (24) (2020) 1–53, https://doi.org/10.3390/ijms21249739.
[27] F.G. Spinale, et al., A matrix metalloproteinase induction/activation system exists in the human left ventricular myocardium and is upregulated in heart failure, Circulation 102 (16) (2000) 1944–1949, https://doi.org/10.1161/01.CIR.102.16.1944.
[28] M.P. Hudson, et al., Effects of selective matrix metalloproteinase inhibitor (PG-116800) to prevent ventricular remodeling after myocardial infarction. Results of the PREMIER (prevention of myocardial infarction early remodeling) trial, J. Am. Coll. Cardiol. 48 (1) (2006) 15–20, https://doi.org/10.1016/j.jacc.2006.02.055.
[29] B.J. Dezube, S.E. Krown, J.Y. Lee, K.S. Bauer, D.M. Aboulafia, Randomized phase II trial of matrix metalloproteinase inhibitor COL-3 in AIDS-related Kaposi's sarcoma: an AIDS malignancy consortium study, J. Clin. Oncol. 24 (9) (2006) 1389–1394, https://doi.org/10.1200/JCO.2005.04.2614.
[30] A. Tessone, et al., Effect of matrix metalloproteinase inhibition by doxycycline on myocardial healing and remodeling after myocardial infarction, Cardiovasc. Drugs Ther. no. Mi (2006) 383–390, https://doi.org/10.1007/s10557-005-5201-6.
[31] B. Peña, et al., Injectable hydrogels for cardiac tissue engineering, Macromol. Biosci. 18 (6) (2018) 1–22, https://doi.org/10.1002/mabi.201800079.
[32] S.D. Anker, et al., A prospective comparison of alginate-hydrogel with standard medical therapy to determine impact on functional capacity and clinical outcomes in patients with advanced heart failure (AUGMENT-HF trial), Eur. Heart J. 36 (34) (2015) 2297–2309, https://doi.org/10.1093/eurheartj/ehv259.
[33] L. Stapleton, Y. Zhu, Y. Ping J. Woo, E. Appel, Engineered biomaterials for heart disease, Curr. Opin. Biotechnol. 66 (2020) 246–254, https://doi.org/10.1016/j.copbio.2020.08.008.
[34] C. Fan, et al., Nanoparticle-mediated drug delivery for treatment of ischemic heart disease, Front. Bioeng. Biotechnol. 8 (June) (2020) 1–13, https://doi.org/10.3389/fbioe.2020.00687.
[35] E. Ruvinov, I. Freeman, R. Fredo, S. Cohen, Spontaneous Coassembly of biologically active nanoparticles via affinity binding of heparin-binding proteins to alginate-sulfate, Nano Lett. 16 (2) (Feb. 2016) 883–888, https://doi.org/10.1021/acs.nanolett.5b03598.
[36] I. Freeman, A. Kedem, S. Cohen, The effect of sulfation of alginate hydrogels on the specific binding and controlled release of heparin-binding proteins, Biomaterials 29 (22) (2008) 3260–3268, https://doi.org/10.1016/j.biomaterials.2008.04.025.
[37] M. Goldshtein, S. Shamir, E. Vinogradov, A. Monsonego, S. Cohen, Co-assembled Ca2+ alginate-sulfate nanoparticles for intracellular plasmid DNA delivery, Mol. Ther. - Nucleic Acids 16 (June) (2019) 378–390, https://doi.org/10.1016/j.omtn.2019.03.006.
[38] E. Ruvinov, S. Cohen, Alginate biomaterial for the treatment of myocardial infarction: Progress, translational strategies, and clinical outlook- from ocean algae to patient bedside, Adv. Drug Deliv. Rev. 96 (2016) 54–76, https://doi.org/10.1016/j.addr.2015.04.021.
[39] Y. Sapir, O. Kryukov, S. Cohen, Integration of multiple cell-matrix interactions into alginate scaffolds for promoting cardiac tissue regeneration, Biomaterials 32 (7) (2011) 1838–1847, https://doi.org/10.1016/j.biomaterials.2010.11.008.
[40] Alan D. Cardin, H.J.R. Weintraub, Molecular modeling of protein-glycosaminoglycan interactions, Arterioscler. An Off. J. Am. Hear. Assoc. 9 (1) (1989) 21–32, https://doi.org/10.1161/01.ATV.9.1.21.
[41] E. Ruvinov, J. Leor, S. Cohen, The promotion of myocardial repair by the sequential delivery of IGF-1 and HGF from an injectable alginate biomaterial in a model of acute myocardial infarction, Biomaterials 32 (2) (2011) 565–578, https://doi.org/10.1016/j.biomaterials.2010.08.097.
[42] D. Verma, N. Gulati, S. Kaul, S. Mukherjee, U. Nagaich, Protein based nanostructures for drug delivery, J. Pharm. 2018 (2018) 1–18, https://doi.org/10.1155/2018/9285854.
[43] G. Yosef, H. Hayun, N. Papo, Simultaneous targeting of CD44 and MMP9 catalytic and hemopexin domains as a therapeutic strategy, Biochem. J. 478 (5) (2021) 1139–1157, https://doi.org/10.1042/BCJ20200628.
[44] V. Arkadash, et al., Development of high affinity and high specificity inhibitors of matrix metalloproteinase 14 through computational design and directed evolution, J. Biol. Chem. 292 (8) (2017) 3481–3495, https://doi.org/10.1074/jbc.M116.756718.
[45] N. Sela-Passwell, et al., Antibodies targeting the catalytic zinc complex of activated matrix metalloproteinases show therapeutic potential, Nat. Med. 18 (1) (2012) 143–147, https://doi.org/10.1038/nm.2582.
[46] H. Frankowski, Y.H. Gu, J.H. Heo, R. Milner, G.J. Del Zoppo, Use of gel Zymography to examine matrix metalloproteinase (gelatinase) expression in brain tissue or in primary glial cultures, Methods Mol. Biol. 814 (2012) 221–233, https://doi.org/10.1007/978-1-61779-452-0_15.
[47] M. Ozols, et al., Predicting proteolysis in complex proteomes using deep learning, Int. J. Mol. Sci. Artic. (2021), https://doi.org/10.3390/ijms22063071.
[48] B. Polyak, Synthesis and characterization of a biotin-alginate conjugate and its application in a biosensor construction, Biomacromolecules 6 (6) (2005) 3315–3318, https://doi.org/10.1021/bm050339j.
[49] L.E. Weil, et al., Oligomerization and auto-methylation of the human lysine methyltransferase SETD6, J. Mol. Biol. 430 (21) (2018) 4359–4368, https://doi.org/10.1016/j.jmb.2018.08.028.
[50] S.W. Provencher, A constrained regularization method for inverting data represented by linear algebraic or integral equations, Comput. Phys. Commun. 27 (3) (1982) 213–227, https://doi.org/10.1016/0010-4655(82)90173-4.
[51] J. Ilavsky, P.R. Jemian, Irena: tool suite for modeling and analysis of small-angle scattering, J. Appl. Crystallogr. 42 (2) (2009) 347–353, https://doi.org/10.1107/S0021889809002222.
[52] H.B. Stuhrmann, Small-angle scattering of X-rays, Prog. Cryst. Growth Charact. 18, no. C (1989) 1–19, https://doi.org/10.1016/0146-3535(89)90023-3.
[53] P. Bankhead, et al., QuPath: open source software for digital pathology image analysis, Sci. Rep. 7 (1) (2017) 1–7, https://doi.org/10.1038/s41598-017-17204-5.
[54] H. Nagase, R. Visse, G. Murphy, Structure and function of matrix metalloproteinases and TIMPs, Cardiovasc. Res. 69 (3) (2006) 562–573, https://doi.org/10.1016/j.cardiores.2005.12.002.
[55] Y. Tabata, Y. Ikada, Protein release from gelatin matrices, Adv. Drug Deliv. Rev. 31 (1998) 287–301, https://doi.org/10.1016/S0169-409X(97)00125-7.
[56] S.M. Ahsan, C.M. Rao, The role of surface charge in the desolvation process of gelatin: implications in nanoparticle synthesis and modulation of drug release, Int. J. Nanomedicine 12 (2017) 795–808, https://doi.org/10.2147/IJN.S124938.
[57] C. Claaßen, L. Sewald, G.E.M. Tovar, K. Borchers, Controlled release of vascular endothelial growth factor from heparin-functionalized gelatin type a and albumin hydrogels, Gels 3 (4) (2017) 35, https://doi.org/10.3390/gels3040035.
[58] S. Young, M. Wong, Y. Tabata, A.G. Mikos, Gelatin as a delivery vehicle for the controlled release of bioactive molecules, J. Control. Release 109 (1) (2005) 256–274, https://doi.org/10.1016/j.jconrel.2005.09.023.
[59] J. Ishihara, et al., Laminin heparin-binding peptides bind to several growth factors and enhance diabetic wound healing, Nat. Commun. no. 2018 (2018), https://doi.org/10.1038/s41467-018-04525-w.
[60] A.G. Kikhney, D.I. Svergun, A practical guide to small angle X-ray scattering (SAXS) of flexible and intrinsically disordered proteins, FEBS Lett. 589 (19) (2015) 2570–2577, https://doi.org/10.1016/j.febslet.2015.08.027.
[61] S. Pabisch, B. Feichtenschlager, G. Kickelbick, H. Peterlik, Effect of interparticle interactions on size determination of zirconia and silica based systems - a comparison of SAXS, DLS, BET, XRD and TEM, Chem. Phys. Lett. 521 (2012) 91–97, https://doi.org/10.1016/j.cplett.2011.11.049.
[62] A. Schwamberger, et al., Combining SAXS and DLS for simultaneous measurements and time-resolved monitoring of nanoparticle synthesis, Nucl. Instruments Methods Phys. Res. Sect. B Beam Interact. with Mater. Atoms 343 (2015) 116–122, https://doi.org/10.1016/j.nimb.2014.11.049.
[63] O. Glatter, Scattering Methods and their Application in Colloid and Interface Science, Elsevier, 2018.
[64] J.T. Edward, Molecular volumes and the stokes-Einstein equation, J. Chem. Educ. 47 (4) (Apr. 1970) 261, https://doi.org/10.1021/ed047p261.
[65] Q. Gan, T. Wang, Chitosan nanoparticle as protein delivery carrier-systematic examination of fabrication conditions for efficient loading and release, Colloids Surf. B: Biointerfaces 59 (1) (2007) 24–34, https://doi.org/10.1016/j.colsurfb.2007.04.009.
[66] C. Berkland, M. King, A. Cox, K. Kim, D.W. Pack, Precise control of PLG microsphere size provides enhanced control of drug release rate, J. Control. Release 82 (1) (2002) 137–147, https://doi.org/10.1016/S0168-3659(02)00136-0.

[67] T. Zhao, et al., Reactive oxygen species-based nanomaterials for the treatment of myocardial ischemia reperfusion injuries, Bioact. Mater. 7 (2022) 47–72, https://doi.org/10.1016/j.bioactmat.2021.06.006.
[68] L. Ruan, et al., Progress in the application of sustained-release drug microspheres in tissue engineering, Mater. Today Bio 16, no. July (2022), 100394, https://doi.org/10.1016/j.mtbio.2022.100394.
[69] O. Perelshtein Brezinov, R. Klempfner, S. Ben Zekry, I. Goldenberg, R. Kuperstein, Prognostic value of ejection fraction in patients admitted with acute coronary syndrome: a real world study, Med. (United States) 96 (9) (2017), https://doi.org/10.1097/MD.0000000000006226.
[70] A. Aimo, H.K. Gaggin, A. Barison, M. Emdin, J.L. Januzzi, Imaging, biomarker, and clinical predictors of cardiac remodeling in heart failure with reduced ejection fraction, JACC Hear. Fail. 7 (9) (2019) 782–794, https://doi.org/10.1016/j.jchf.2019.06.004.
[71] E.M. Wilson, et al., Region- and type-specific induction of matrix metalloproteinases in post-myocardial infarction remodeling, Circulation 107 (22) (2003) 2857–2863, https://doi.org/10.1161/01.CIR.0000068375.40887.FA.
[72] J. Sundström, et al., Relations of Plasma Matrix Metalloproteinase-9 to Clinical Cardiovascular Risk Factors and Echocardiographic Left Ventricular Measures, 2004, pp. 2850–2856, https://doi.org/10.1161/01.CIR.0000129318.79570.84.
[73] J. Hogwood, et al., The effect of increasing the sulfation level of chondroitin sulfate on anticoagulant specific activity and activation of the kinin system, PLoS One 13 (3) (2018) 1–13, https://doi.org/10.1371/journal.pone.0193482.
[74] T.K. Kishimoto, et al., Contaminated heparin associated with adverse clinical events and activation of the contact system, N. Engl. J. Med. 358 (23) (2008) 2457–2467, https://doi.org/10.1056/nejmoa0803200.